Climate Dynamics (2025) 63:58
https://doi.org/10.1007/s00382-024-07549-9

ORIGINAL ARTICLE

Seasonality of feedback mechanisms involved in Pacific coastal Niño events

Daniel Rudloff[1] · Joke F. Lübbecke[1] · Sebastian Wahl[1]

Received: 14 March 2024 / Accepted: 9 December 2024

Abstract
The 2017 Pacific Coastal Niño Event was the strongest of its type. It caused torrential rainfall and devastating flooding in Peru and Ecuador and thus rapidly caught the attention of the scientific community. From reanalysis data, three similar events, occurring in 2008, 2012 and 2014, are identified which are however all weaker, peaked later during the year and led to very little socioeconomic impact. This study focuses on the role of seasonality for the evolution and impact of Coastal Niño events. Reanalysis products as well as historical simulations from a coupled climate model and targeted model sensitivity experiments are utilized to assess the seasonal varying contributions of surface heat fluxes, horizontal advection and subsurface processes to the modulation of sea surface temperatures off the Peruvian coast. As the atmospheric conditions underlay a strong seasonal cycle with convection only occurring between December and April, warm events in this season are shown to lead to stronger precipitation anomalies. Pacific coastal Niño events in general are shown to be primarily forced via oceanic processes, but in individual cases local atmospheric forcing plays an important role. However, there is a very high variability between the individual events, with especially the 2017 event standing out due to its forcing, timing, strength and associated precipitation response.

Keywords Coastal Niño · Eastern tropical Pacific · Ocean-atmosphere interaction · Partial coupling

1 Introduction

In February 2017, Sea Surface Temperature (SST) anomalies of more than 5 K were recorded at the coast of Peru (Echevin et al. 2018) causing strong anomalous rainfall and devastating flooding in the otherwise arid coastal region. Such warm anomalies are usually connected to the El Niño-Southern Oscillation (ENSO) and especially its warm phase (El Niño) characterised by an equatorial Pacific-wide warming. The warming in 2017, however, was confined to the coast with no significant SST anomalies in the central-to-eastern equatorial Pacific (Fig. 1). While the impact of SST anomalies on local rainfall especially during boreal spring is well established, the mechanisms behind such strong warm events are still a subject of discussion. Therefore, we need to gain further understanding of those events and especially their seasonality.

The coastal region off Peru (0–15°S) is influenced by both the equatorial and coastal current systems. The latter includes the northward alongshore Peruvian Coastal Current at the surface, which transports cold, recently upwelled waters into the region. These waters enter the equatorial current system and are transported westward by the southern South Equatorial Current at around 5°S. Inflow from the northern hemisphere across the equator is minimal as the northern South Equatorial Current is located just north of the equator transporting northern hemisphere waters westward and thus only marginally entering the region of interest (Montes et al. 2010 and references therein). In the subsurface, equatorial currents such as the Equatorial Undercurrent and the Southern Subsurface Countercurrent transport warm waters eastward into the coastal region, which is then advected southward by the Peru Chile Countercurrent and the Peru Chile Undercurrent. The region also features the strongest eastern boundary upwelling system (Chavez and Messié 2009), where surface temperatures are lowered by vertical advection of colder subsurface waters.

✉ Daniel Rudloff
drudloff@geomar.de

[1] GEOMAR Helmholtz Centre for Ocean Research Kiel, Kiel, Germany

Published online: 23 December 2024

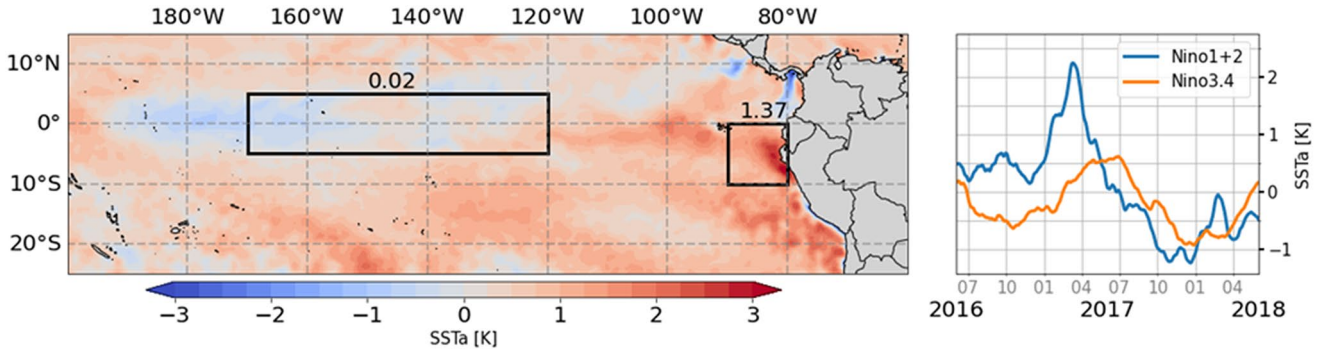

Fig. 1 Sea surface temperature anomalies during February 2017 from NOAA OISST v2 (left) and time series of Niño1 + 2 and Niño3.4 SST anomalies (right). The solid rectangles indicate the Niño1 + 2 and Niño3.4 regions. Numbers display area-averaged SST anomalies for the respective box

The upwelling is mainly driven by the northward alongshore winds (Brink et al. 1983). This leads to relatively cool surface waters compared to other tropical regions and contributes to the arid conditions. Even during the seasonal peak in March, the SST is still lower than the convective threshold for tropical regions (~27 °C; Xie and Philander 1994). Atmospheric convection mainly occurs in the intertropical convergence zone (ITCZ), which is located north of the equator during the whole year. A weaker secondary ITCZ develops at around 5°S in March and April east of 150°W (Zhang 2001). Hence, the far eastern equatorial Pacific experiences the presence of different cloud patterns, including low stratiform clouds as well as high convective clouds. The distinctive radiative forcing of both cloud types further modulates SST variations (Chung-Chun Ma et al. 1996; Cronin et al. 2006).

The pronounced SST anomalies observed in 2017 in the Niño1 + 2 region (90°W-80°W;0–10°S) are the fourth strongest on record, with higher anomalies only observed during the major El Niño events in 1983, 1998 and 2016. These basin-wide events, defined by SST anomalies in the Niño3.4 region (170°W-120°W; 5°N-5°S), have been studied extensively. The theoretical background and forcing mechanisms of El Niño events are well described in the literature (e.g. Timmermann et al. 2018; Neelin et al. 1998; Harrison and Larkin 1998). Westerly wind bursts in the western equatorial Pacific excite downwelling equatorial Kelvin waves which propagate eastward along the equator, causing an initial warming in the eastern equatorial Pacific. This warming in turn influences the Walker circulation and causes further weakening of the equatorial easterlies, which marks the beginning of the Bjerknes Feedback (Bjerknes 1969). The knowledge of these mechanisms allows the prediction of El Niño events with a lead time of several months. This was not the case for the strong coastal warming of 2017, which took place without a corresponding warming in the equatorial Pacific. This event was not predicted, further enhancing its socioeconomic impacts (Ramírez and Briones 2017).

There are several forcing mechanisms for the 2017 event proposed in recent studies, which however do not fully agree with each other. Garreaud (2018) found little contribution by Kelvin waves but instead attributed the warming to a relaxation of the south-easterly trade winds at the coast and the following weakening of the coastal upwelling and evaporative cooling. Local atmospheric forcing is also identified as the main driver by Echevin et al. (2018) who showed that the initial warming was caused by surface fluxes and enhanced by wind stress curl-induced weakened entrainment. Other studies suggest that the role of equatorial Kelvin waves is of similar amplitude (Zhao and Karamperidou 2022; Peng et al. 2019).

Extreme coastal Niño events accompanied by neutral or negative SST anomalies in the central Pacific as in 2017 are rare and the only other extreme events mentioned in the literature occurred in 1891 and 1925 (Echevin et al. 2018). Hardly any information is available for 1891, but the warming from February to April 1925 is well described in Takahashi and Martínez (2019). Similar to 2017 it was accompanied by neutral conditions in the central Pacific but in contrast to 2017, this event developed into a basin-wide warming in the following boreal winter (Lübbecke et al. 2019). The forcing was associated with northerly wind anomalies along the coast and a strengthening of the southern branch of the ITCZ. Both events occurred during the annual peak of SST and provoked non-linear feedbacks, leading to a rapid onset of strong anomalies. Similar but less extreme coastal Niños were observed in 2008 and 2014 (Hu et al. 2019). Due to their lack of rainfall anomalies and impacts on society, they are not as extensively studied as the 2017 event. Hu et al. (2019) suggest that in 2014 remote equatorial forcing caused the warming while in 2008 local wind anomalies similar to 2017 were at play. Coastal warmings caused by equatorial Kelvin waves were also present in 1974 and 1975 (McPhaden et al. 2015), but they were too weak and too short to be recognized as coastal Niños in recent studies.

In this study, we revisit the 2017 event and compare it with other coastal warm events from observational records and as simulated by a fully coupled climate model, to compare involved mechanisms and feedbacks. We particularly highlight the role of seasonality, not only for the SST anomalies causing strong rainfall but also for the development of the warming itself. Hence, after the data and methodology are presented in Sect. 2, the seasonality of terms modulating SST as well as the cloudiness is investigated in Sect. 3. Afterwards, coastal Niño events from observations and model simulations are analysed in Sect. 4. In Sect. 5 we take a closer look at selected mechanisms by analysing targeted model experiments with respect to the strength of mechanisms and feedbacks during different seasons, followed by a summary and discussion of the main findings in Sect. 6.

2 Data and methods

2.1 Reanalysis products

Atmospheric variables, such as wind speed, cloudiness and surface heat fluxes are obtained from the fifth-generation ECMWF reanalysis [ERA5, Hersbach et al. 2023]. This data is available hourly on a 0.25° x 0.25° horizontal grid. For this study, daily averages are used. Three-dimensional oceanic variables such as subsurface temperature and velocities are taken from the CMEMS Global Ocean Reanalysis (GLORYS, https://doi.org/10.48670/moi-00024) distributed by E.U. Copernicus Marine Service Information, available on a 0.25° x 0.25° grid with 75 vertical levels and daily temporal resolution. From both data sets, the common period from 1993 to 2020 is used.

2.2 FOCI model

We use the Flexible Ocean Climate Infrastructure (FOCI), a fully coupled ocean-atmosphere-land model (Matthes et al. 2020). The ocean component is based on the Nucleus for European Modelling of the Ocean (NEMO) version 3.6, ocean sea-ice model (Madec 2016). The Jena Scheme for Biosphere Atmosphere Coupling in Hamburg (JSBACH, Reick et al. 2013; Brovkin et al. 2009) is used for lower atmospheric boundary conditions over land. For the atmospheric component, the European Centre Hamburg general circulation model (ECHAM6, Stevens et al. 2013; Müller et al. 2018) with the T63L95 configuration is used, corresponding to approximately 1.8° in grid point space. The ocean component has a 0.5° horizontal resolution and 46 depth levels with a vertical grid spacing increasing from 6 m at the surface to 250 m at depth with the application of partial cells at the seafloor (ORCA05 configuration; Barnier et al. 2006; Biastoch et al. 2008). The surface boundary conditions retrieved from ECHAM6 are coupled to the ocean model via the OASIS3-MCT coupler (Valcke 2013). These include heat and freshwater fluxes as well as wind stress, in which calculation ocean current feedbacks are included.

In this study three runs with identical configurations and historical atmospheric boundary conditions, spanning the years 1850 to 2013, are analysed. The initial states of the ocean and atmosphere are taken from a 1,500-year-long FOCI control simulation described in Matthes et al. (2020).

2.3 Model sensitivity experiments

In order to analyse the effect of the seasonality, we conduct a set of 2-year-long sensitivity experiments, in which we force a coastal warming off Peru by locally prescribing a wind stress forcing. The prescribed wind stress is based on a composite of coastal warm events from a 3000-year-long pre-industrial control run (piCtrl). As described by Thoma et al. (2015), we calculate the wind stress anomalies and add them to the climatology utilizing a partial coupling approach. Thereby, the forcing only influences the momentum flux but not the surface heat fluxes, as the winds used for the heat flux calculation are not directly affected by the applied forcing. Applied anomalies are southward, i.e. a weakening of the southerly trades, within the Niño1+2 region and decrease south of 10°S. The forcing is applied in the coastal area (0°-15°S; 85°W-75°W) with a 5° wide transition zone where the forcing is linearly decreasing. The whole forcing is applied for 40 days with a 5-day period during which the forcing over the whole area is gradually increasing (decreasing) at the beginning (end). In total we conduct four sets of experiments by applying the forcing either on the 10th (JAN) or 100th (APR) day of the year using two different starting years for each experiment from the piCtrl run. During both years the equatorial Pacific was in a neutral state with SST anomalies in the Niño3.4 and Niño1+2 regions close to 0. After the forcing period, the forcing is turned off and the model can evolve freely. For each set of experiments, eleven ensemble members are simulated as well as an eleven-ensemble control simulation without any prescribed wind forcing.

2.4 Mixed layer heat budget

To determine the importance of different processes for the temperature evolution in the Coastal Niño area, a mixed layer heat budget is calculated as:

$$\frac{\partial \mathrm{T}}{\partial \mathrm{t}} = \mathrm{SHF} + \mathrm{ADV} + \mathrm{subsurface}$$

describing the temporal change in the mixed layer temperature (T) due to surface heat fluxes (SHF), horizontal ocean advection (ADV) and oceanic subsurface processes (subsurface) with

$$SHF = \frac{Q_{surf}}{\rho\, C_p h}, \quad ADV = \int_0^h - u\frac{dT}{dx} - v\frac{dT}{dy}dz$$

where h is the mixed layer depth, ρ and C_p are the density (1025 kg/m³) and specific heat capacity of seawater (4000 J K^{-1} kg^{-1}), respectively, and u and v are the zonal and meridional ocean velocities.

The net surface heat flux (Q_{surf}) consists of the latent heat flux, the sensible heat flux, the longwave radiation and the shortwave radiation. For shortwave radiation, only the part which is absorbed within the mixed layer is considered. This part is calculated as $Q_{abs} = SWR*1 - 0.47\, e^{h/15}$ (Foltz et al. 2020), where SWR is the net surface shortwave radiation and h is the mixed layer depth in meters. The horizontal advection is calculated for each grid point as the integral over the mixed layer of the product of horizontal velocities and temperature gradient. Similar to Peng et al. (2019) the subsurface term is defined as the residual and includes processes like vertical entrainment and mixing through the mixed layer base. For further insights into this term, the mean upward velocities (UPW) and the vertical temperature gradient (dT/dz) are calculated. UPW is the area mean of all upward velocities at the base of the mixed layer plus the temporal change of the mixed layer depth. The vertical temperature gradient is calculated as the difference between the temperature 5 m below the mixed layer and the mean mixed layer temperature. Mixed layer depth is determined by a temperature difference of 0.2 K relative to the surface temperature. For the mixed layer heat budget, the Niño1 + 2 region is extended eastward to the South American coast to capture coastal processes. This region will be referred to as the coastal Niño1 + 2 region (0°-10°S; 90°W – coast).

2.5 Definition of coastal Niño events

Coastal Niño events have been defined by different criteria in the literature. The Comité encargado del Estudio Nacional del Fenómeno El Niño (ENFEN, Peru) uses a 3-month-running-mean Niño1 + 2 SST index (L'Heureux et al. 2017). Ramírez and Briones (2017) discussed the shortcomings of this index for the 2017 event, as it can neither capture the full magnitude nor is it suitable for such a rapidly developing event. Therefore, we propose here different criteria to determine a Coastal Niño event using daily SST anomalies (SSTa), roughly following Lübbecke et al. (2019). As we are looking for events without any basin-wide anomalies we also include the Niño3.4 SSTa. For an event to be considered as a Coastal Niño in this study the 30-day running mean SSTa in the Niño1 + 2 region has to exceed its standard deviation, while it must not exceed 70% of its standard deviation in the Niño3.4 region. Further, the difference between the Niño1 + 2 SSTa and Niño3.4 SSTa has to be at least 0.5 K. All three conditions have to be fulfilled for 50 consecutive days. We further focus on events that do not show any warming in the central Pacific directly before or after the coastal warming. These will be referred to as Stand Alone Coastal Niño Events (Lübbecke et al. 2019). All events are separated into three phases, the build-up, the peak and the decay phase. The peak phase is characterized by Niño1 + 2 SSTa higher than 80% of the maximum reached in each respective event. The build-up phase describes the period before the peak phase with positive and increasing Niño1 + 2 SSTa, while the decay phase subsequently follows the peak phase and is defined by positive but decreasing Niño1 + 2 SSTa.

3 Seasonal cycle

In this section, we examine which terms are dominating the mixed layer temperature evolution throughout the year in order to assess how certain feedbacks and interactions might differ between the seasons. It further serves as an important comparison between model and reanalysis products, as differences in feedbacks might be caused by different climatologies.

In the coastal Niño1 + 2 region, the climatologically highest SST is reached in March. Compared to the reanalysis, the model runs show a consistently higher SST during the whole warm season (Fig. 2a). However, the subsequent cooling is also stronger leading to comparable SST from May to August. Minimum temperatures are reached already in August in the model, while reanalysis data shows a minimum in September. To better understand which processes contribute to the seasonal changes, a mixed-layer heat budget is calculated (Fig. 2b, c, d). Surface heat fluxes warm the region throughout the year while subsurface processes provide the main cooling mechanism. The generally too warm upwelling region is a common bias in global climate models which has various reasons (Richter 2015). In the following, we focus on the discrepancies of the processes responsible for seasonal cooling and warming.

The reanalysis products present the strongest warming by surface heat fluxes during the warming phase in boreal winter and the weakest in boreal summer. Subsurface cooling, which mainly consists of the upwelling of cold subsurface waters and vertical mixing through the mixed layer base, is strong throughout the year with its highest values after the seasonal peak in SST when upwelling velocities

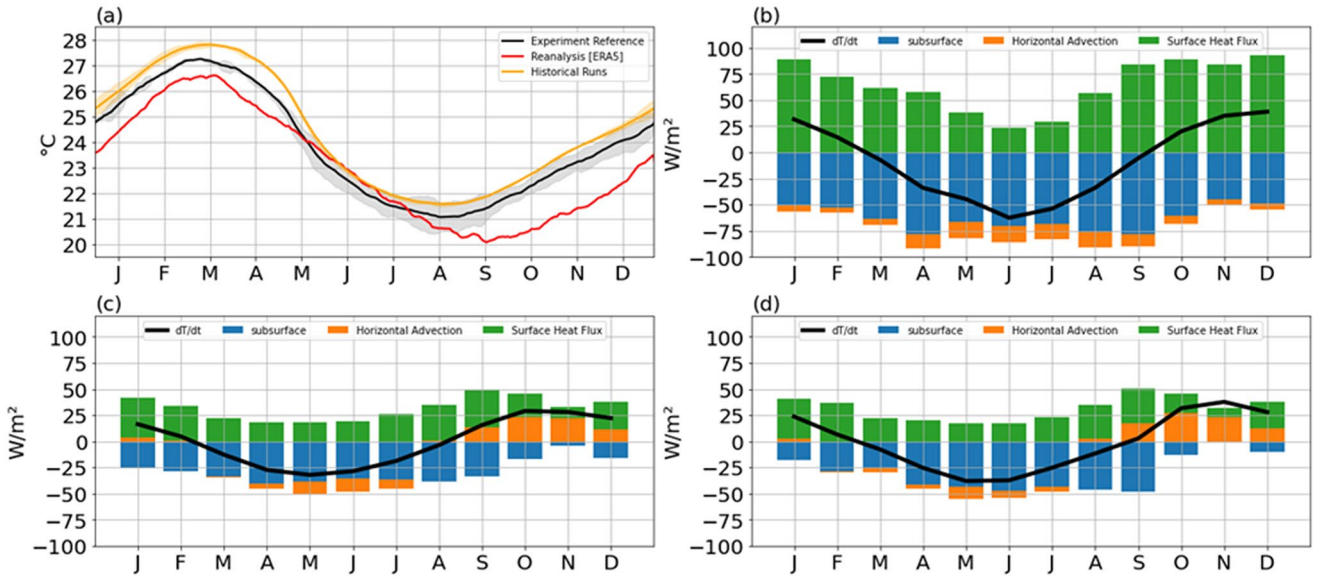

Fig. 2 Seasonal cycle for the coastal Niño 1+2 region (0–10°S;90°W - coast) of (**a**) SST and Mixed Layer Heat budget terms based on (**b**) ERA5 and GLORYS reanalysis, (**c**) mean of all three historical model runs and (**d**) reference runs for model sensitivity experiments. Shading in (**a**) indicates two standard deviations

are strongest. During the time of highest SST, the vertical temperature gradient is strongest causing strong subsurface cooling even with lower upwelling velocities. Horizontal advection provides additional cooling of 10–20 W/m² throughout the whole year (Fig. 2b).

The heat budgets calculated from the model simulations (Fig. 2c and d) resemble each other. However, they display some differences to the reanalysis data. First, the magnitude of the surface heat fluxes and the subsurface term is much smaller and second, during the seasonal warming from August to January the horizontal advection term becomes positive, while it is negative throughout the whole year in the reanalysis data. Discrepancies in horizontal advection are caused by an artificial southward coastal current in the model, transporting warmer waters from north of the equator into the Niño1+2 region. This current is visible along the coast, even at the southern boundary of the Nino1+2 region where reanalysis products indicate a northward inflow of colder waters with the Peru-Chile Current. In the model simulations, this inflow of colder waters is shifted offshore, balancing the error to some extent. The biggest differences are found north of 5°S in the coastal region. During the first half of the year, the alongshore northward advection is rather small and hence the relatively poor representation in the model runs does not cause major offsets, whereas from July to December the biases are much larger for the meridional advection at both the northern and southern boundary of the Niño1+2 region. Additionally, the offshore transport is underestimated in the model throughout the year, which further contributes to too little oceanic cooling in the Niño1+2 region. These biases in horizontal advection are a general problem in global climate models (e.g. de Szoeke et al. 2010). The poor representation of coastal currents in the model thus does not allow for a detailed analysis of the advection, especially in the second half of the year. However, general changes in advection are still reasonable for the first half of the year, which is the focus of our study.

The lower magnitude of the surface heat fluxes in the model can be explained by the general warm bias of the coastal region, which increases outgoing longwave radiation and evaporation and thus dampens the warming by surface heat fluxes. Differences in the seasonal cycle of heat fluxes are further attributed to seasonal differences in the mixed layer depth (MLD). While the mean MLD for the Niño1+2 region in the reanalysis data ranges from 17 m in February and March to about 33 m in August, the model only shows MLD from 13 m in February to 20 m in July. This enhances the part of the shortwave radiation which penetrates through the mixed layer in the model. Further, the latent heat flux is weakest in JJA in the model while they are strongest during these months from reanalysis. In combination, this diminishes the magnitude of the annual cycle of the surface heat flux in the model. Additionally, the surface heat fluxes are strongly influenced by clouds. In the far eastern tropical Pacific the usually biannual cycle of the sun in the tropics is modulated by the cloudiness resulting in an annual cycle of shortwave radiation (Ma et al. 1996). The main features determining the cloud patterns in the tropical Pacific are the cold tongue and the emergence of the double ITCZ in boreal spring. On smaller scales, SST-cloud interactions play an important role.

The total cloud coverage (TCC) in the coastal Niño1+2 region only experiences slight changes throughout the year, ranging from 0.6 in boreal spring to 0.8 in boreal autumn (Fig. 3a and c). The mechanisms creating the clouds however differ between those seasons. For most of the year, subsiding air masses over the stable atmosphere due to relatively low SSTs create low stratiform clouds as described by Ma et al. (1996). During the presence of the double ITCZ in boreal spring, deep convection can be observed also south of the equator (Gu et al. 2005). This leads to TCC being nearly identical to the low cloud coverage (LCC) for most of the year, but differing strongly from January to April when convective clouds are present (Fig. 3a). This seasonality is well captured by the model (Fig. 3c).

Since there are different processes responsible for cloudiness, the relationship between anomalies in SST and cloud coverage varies seasonally. The general correlation of TCC and SST anomalies is around 0.3 in FMA and −0.3 from June to November in the reanalysis data. In the model, the correlation is slightly weaker with 0.2 in FMA and −0.3 during the rest of the year. However, due to the large amount of data considered, the regression values are statistically significant. While in February and March, the regression coefficient of TCC against SST is strongly positive (roughly 5%/K), it is slightly negative throughout most of the year (Fig. 3b and d). Hence, in the climatologically warmest boreal spring, additional warming leads to more convection and subsequently more clouds. As a consequence, less solar radiation reaches the sea surface and dampens the warming. Outside of this convective season, positive SST anomalies warm the cold upwelling water, reducing atmospheric stability and the subsiding of air masses which in turn reduces cloudiness, often referred to as the low cloud cover (LCC) - SST relationship (e.g. Cesana et al. 2019 and reference therein) which is still challenging to simulate even for higher resolution coupled climate models (Moreno-Chamarro et al. 2022). A warming during this season thus leads to a weak but positive shortwave radiation feedback. The seasonality of the regression coefficients is also represented well by the model (Fig. 3d) with a slightly stronger negative correlation between SST and low clouds. However, the LCC-SST relationship only dominates when no deep convection is triggered. February to April are the only months with a positive correlation between TCC which includes LCC and SST, in agreement with the convective season visible from the reanalysis (Fig. 3b, d).

In summary, we find that the mechanisms governing SST changes in the Niño 1+2 region vary over the year. Additionally, the SST-cloud interactions also differ between boreal spring, when atmospheric convection plays an

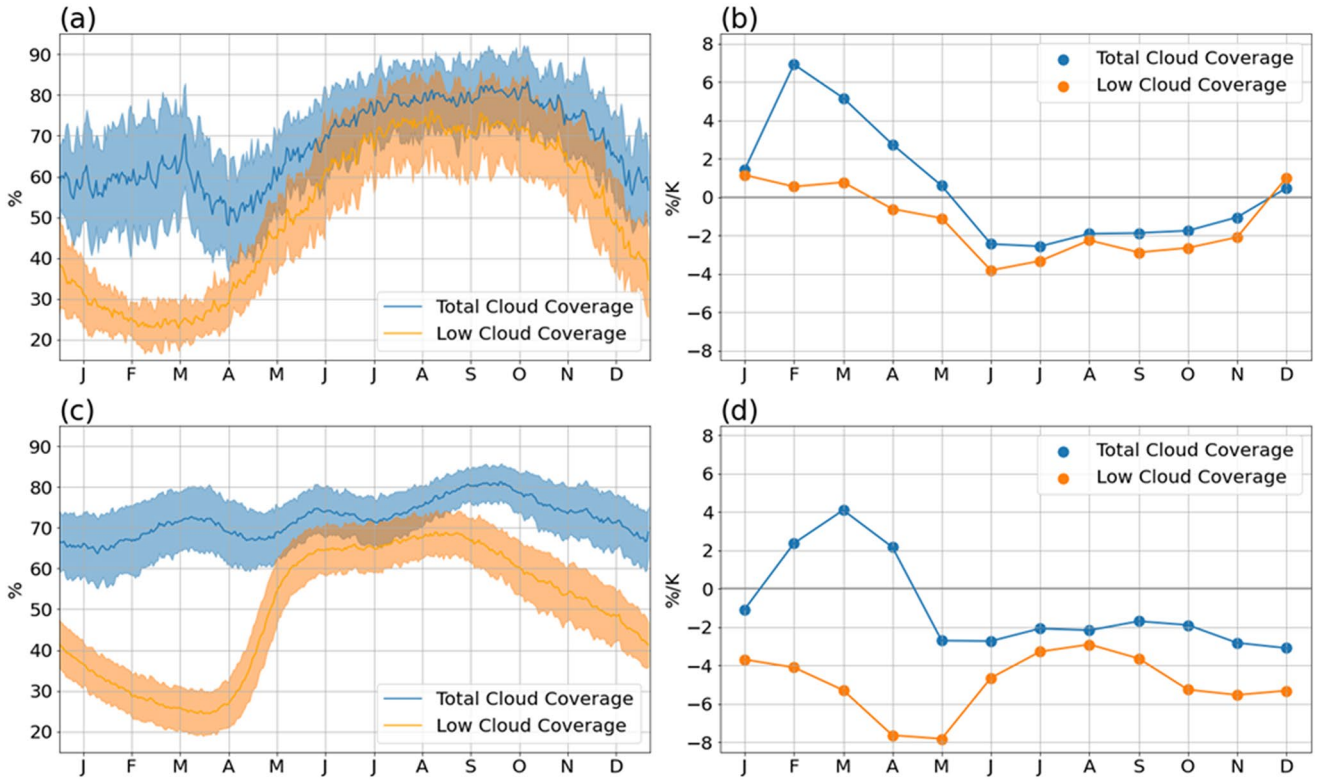

Fig. 3 Seasonal cycle of cloud coverage averaged over the coastal Niño1+2 region (**a**) and linear regression coefficients of cloud coverage on SST anomalies (**b**) for total cloud coverage (blue) and low clouds (orange) based on reanalysis data. (**c**) and (**d**) are the same as (**a**) and (**b**) but from model output

important role and the rest of the year when low stratiform clouds are dominant. This raises the question how this influences the seasonality of coastal Niño events, which are the focus of the next section.

4 Coastal Niño events

Based on the findings in Sect. 3, we here identify and characterise coastal Niño events in our data sets and investigate involved mechanisms with respect to their seasonality.

In the Reanalysis products, four Stand Alone Coastal Niño Events are identified based on the criteria introduced in Sect. 2.5. These events occurred in 2008, 2012, 2014 and 2017. A fifth coastal Niño event occurred in 1998 in the aftermath of the strong basin-wide El Niño of 1997/1998 but is not considered in this study as it is not classified as a Stand Alone event. In the three independent historical FOCI model runs that we analysed, 14 such events occurred. The simulated events display a clear maximum of SSTa in the Niño1 + 2 region, extending along the equator into the central Pacific, but are hardly reaching the Niño3.4 region (Fig. 4a). Compared to the 2017 coastal Niño (Fig. 1) the warming along the coast is more confined to the region north of 10°S and less intense along the Peruvian coast.

As displayed in Fig. 5a, the majority of simulated events peak in boreal winter (DJF) while three of the four observed events have their peak in boreal summer (JJA). The main outlier is the 2017 event which peaked in boreal spring. It is also the strongest of all observed events concerning Niño1 + 2 SSTa. Overall, the events from the reanalysis product are slightly stronger in terms of maximum Niño1 + 2 SSTa (1.93 K compared to 1.54 K) but comparable in duration (79 days) to the ones found in the model simulations (78 days). Due to the high event-to-event variability in terms of timing, duration and intensity, we separate each event into three phases as introduced in Sect. 2.5.

For each phase of each event, the anomalies of all mixed layer heat budget terms are computed. Due to differences in duration and total SSTa change during build-up or decay phases, the contributions are normalised by the sum of all terms and displayed as relative contributions (Fig. 5b-e). For the observed and simulated events, the dominant terms during the build-up phase are horizontal advection and subsurface processes. Surface heat fluxes mostly act as a damping, even during the build-up phase. The only observed event forced by surface heat fluxes is the 2017 event. For the decay of the observed events subsurface terms are consistently the main driver, with very little contribution by surface heat fluxes and horizontal advection. In the model simulations the contributions during the build-up phase agree with the observed ones. However, the decay phase differs strongly. Dominant terms in the model are surface heat fluxes and horizontal advection, while subsurface terms are slowing down the decay.

From the observed events, the 2017 event stands out not only as the strongest but also due to its anomalous atmospheric forcing. In comparison to the other observed events, it occurs much earlier in the year. Correspondingly, the simulated events which show significant forcing by surface heat fluxes also peak in December or January. However, there are also simulated events peaking in December or January without any contribution from surface heat fluxes. For more insights into the effect of seasonality on the effectiveness of wind forcing and possible feedback mechanisms we

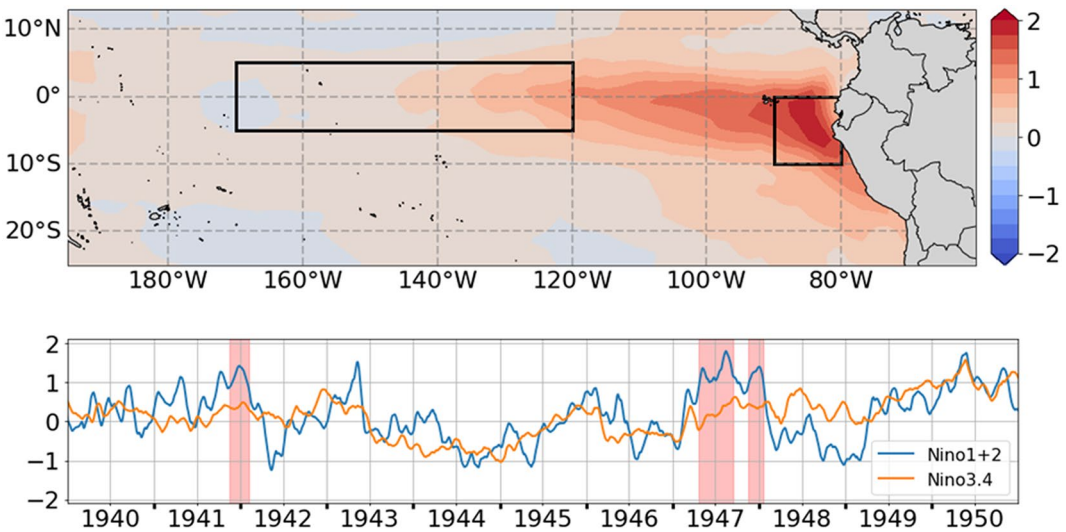

Fig. 4 (Upper) Composite SST Map of Stand Alone Coastal Niño Events from FOCI historical model simulation and (lower) exemplary time series of Niño1 + 2 and Niño3.4 SST anomalies. Red shading indicates Stand Alone Coastal Niño events

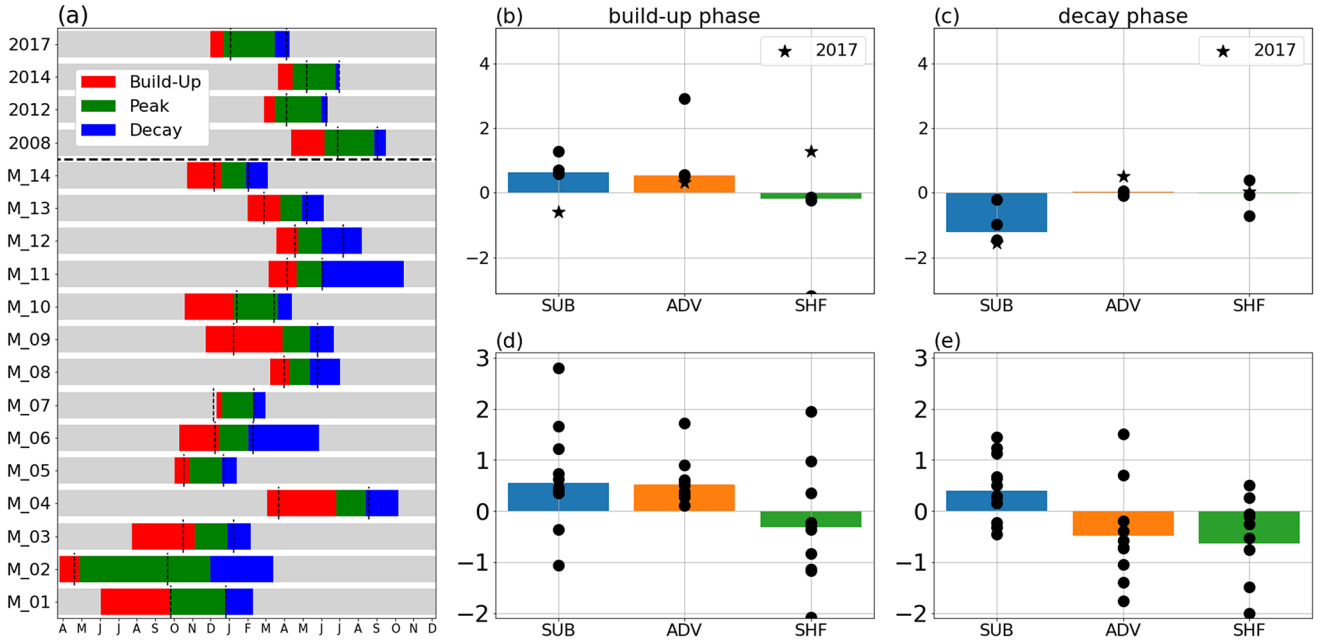

Fig. 5 Timing of all events (**a**) with red, green and blue indicating the build-up, peak and decay phase, respectively. Observed events are denoted by their year while simulated events are numbered consecutively (M_XX). Dashed black lines indicate the time when the criteria for a Coastal Niño are fulfilled. **b**) and **c**) show normalised relative contributions by subsurface processes, horizontal advection and surface heat flux to the respective SST anomaly change for observed events. Coloured bars show the median and black dots indicate single events. **d**) and **e**) are the same as **b**) and **c**) but for the events from historical model runs

conducted model sensitivity experiments which are analysed in the following section.

5 Seasonality of feedback mechanisms

While the observed events happened either during or right after the convective season in FMA, in the historical simulations only a few events did. The peculiarity of the 2017 event also raises the question of whether this is related to the different timing. To address this question and to enlarge the number of events simulated during the same seasons, we conducted model sensitivity experiments. In this section, we present the results of 4 different ensembles containing 11 members each. The forcing (described in Sect. 2.5) is applied either on the 10th or 100th day of the year, i.e. the warming is either forced in January or April and the experiments are labelled JAN and APR accordingly. This is done for two different starting years to further add variations to the results. Hence, there are 22 runs with a warming forced in January and the same amount with a warming forced in April. For each experiment there is a control simulation with an identical configuration but without any forcing applied. The JAN experiments are representative of events occurring during the season when atmospheric deep convection is likely as for example the event in 2017. The timing of the APR events is similar to the ones observed in 2012 and 2014.

In the runs with the wind forcing applied, significant warming is produced at the South American coast for both seasons (Fig. 6). For JAN events, the strongest SST anomalies are located at the South American coast between 5°-15°S, whereas for APR events the warming reaches further north to the equator and westward until 90°W, spanning almost the entire Niño1 + 2 region. As a consequence, the average Niño1 + 2 SST anomalies are much stronger for APR events, even though the local maxima are of similar magnitude.

In the following sections, the oceanic response to the wind stress forcing and the atmospheric response to the initiated warming will be analysed.

5.1 Dynamic response to local wind forcing

In this section, we focus on the period during which the forcing is applied. The different terms influencing mixed layer temperatures are calculated to see how the wind stress forcing produces the coastal warming.

The immediate response to the forcing is a reduction in mixed layer depth, upwelling and subsurface cooling. The warming via horizontal advection is slowly increasing during the forcing period and reaching its maximum towards the end. Warming via subsurface processes is reduced with

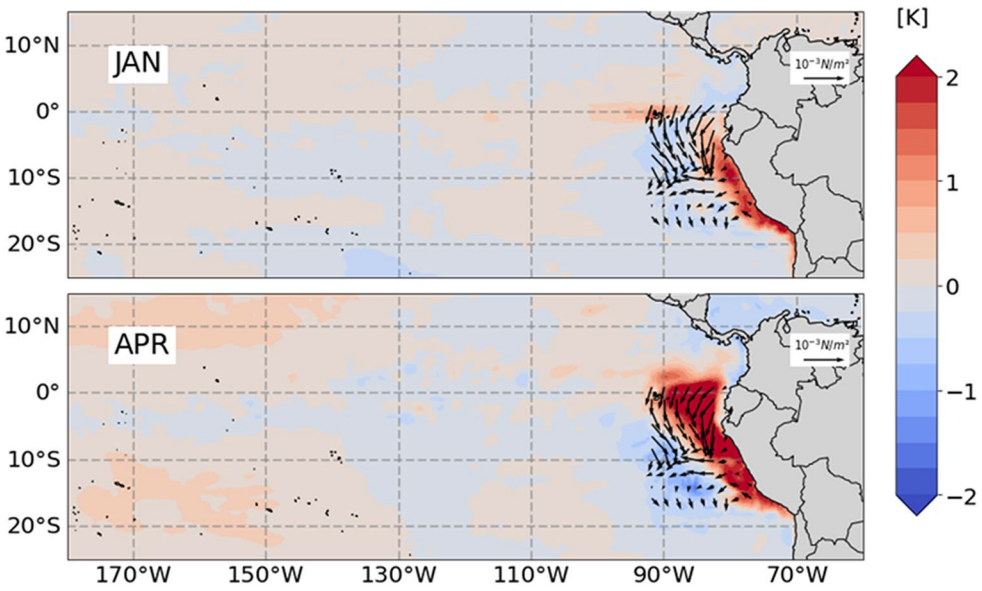

Fig. 6 Ensemble means from model sensitivity experiments displaying SST anomalies for the end of the forcing phase for JAN events (upper) and APR events (lower). Anomalies are averaged over 20 days. Arrows show wind stress anomalies used as a forcing to create coastal warming. Average SST anomalies in the Niño1 + 2 region are 0.54 K for the JAN events and 1.83 K for APR events

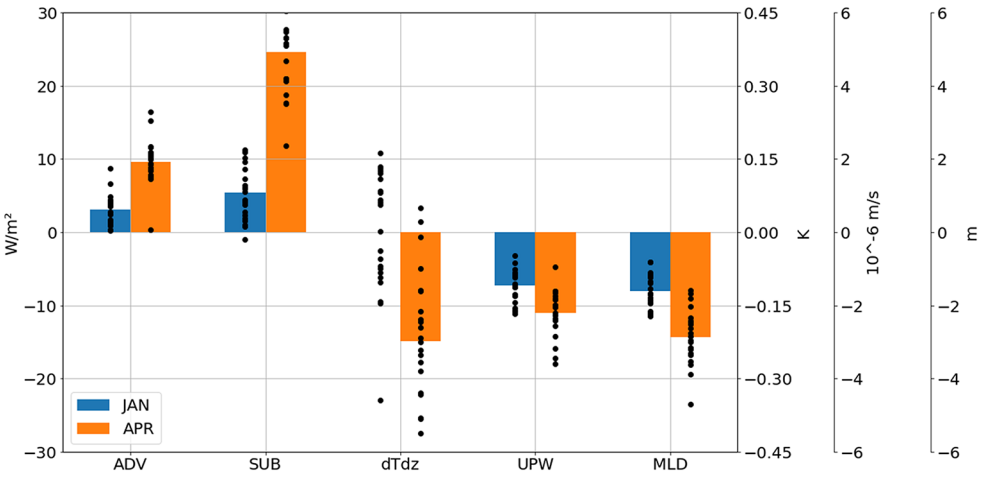

Fig. 7 Averages for horizontal advection (ADV), subsurface processes (SUB), vertical temperature gradient (dTdz), upwelling (UPW) and mixed layer depth (MLD) for the coastal Niño1 + 2 region over the forcing period. Black dots show values for individual ensemble members

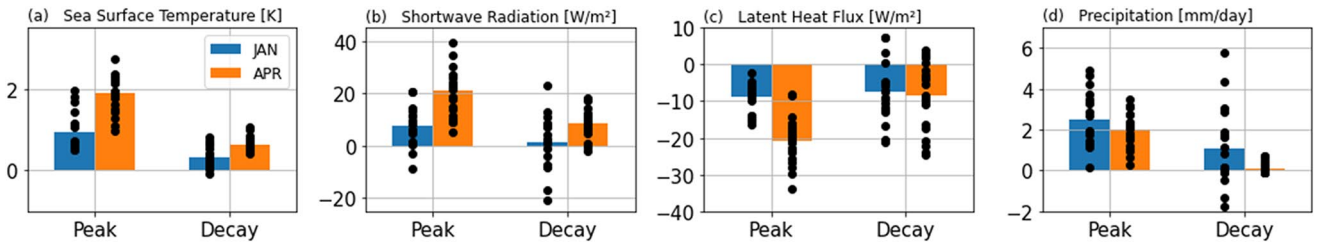

Fig. 8 Averages over the Niño1 + 2 region for **a**) sea surface temperature, **b**) shortwave radiation, **c**) latent heat flux and **d**) precipitation for peak and decay phase for Coastal Niño events from sensitivity experiments. Displayed values are differences between model experiments and respective control runs. Events with a maximum SSTa of less than 0.5 K are excluded. Black dots show values for individual ensemble members

time as the vertical temperature gradient increases due to the surface warming so that the horizontal advection becomes the dominant warming term. Upwelling anomalies and MLD anomalies are constant throughout most of the forcing period.

Even though the main mechanisms causing the warming are the same, there are substantial differences between the two seasons. For the APR events, both the vertical and advective terms are stronger, leading to a stronger surface warming in those experiments (Figs. 7 and 8a). However, in both seasons the wind stress reduction leads to a decrease in MLD and upwelling. These signals are stronger for the APR events by a factor of two (Fig. 7). Differences in the reaction to the wind stress forcing can be attributed to different

background conditions during those seasons as described below.

The JAN period is characterised by seasonally weaker winds and therefore a shallower mixed layer and weaker upwelling to begin with. Further, the vertical temperature gradient and cooling via horizontal advection are weaker. At the same time, the atmospheric heat fluxes are at their maximum. Hence, the heat budget is governed by atmospheric fluxes rather than wind-driven ocean dynamics (Fig. 2b-d). As a consequence, a wind stress weakening can further weaken oceanic cooling and shoal the mixed layer but does not lead to strong SST anomalies, as those are not the terms dominating the temperature evolution during this time.

For the APR period, the situation is very different. Seasonally the SST is decreasing as the surface heat fluxes are weaker and cooling via subsurface processes is dominant (Fig. 2b-d). The deepened mixed layer, stronger upwelling and a stronger vertical temperature gradient all contribute to that. Decreasing the wind stress can substantially slow down the seasonal cooling, leading to strong warm anomalies. The strong signal in dT/dz (Fig. 7) is a consequence of the surface warming rather than a direct reaction to the wind stress forcing. dT/dz mainly depends on mixed layer depth and mixed layer temperature. While for the JAN events, the mixed layer shoaling and warming cancel each other out, for the APR events the warming dominates and creates a stronger vertical temperature gradient.

5.2 Atmospheric response to initial warming

Once there is a substantial warming of the surface ocean, the atmosphere reacts to this, potentially resulting in feedback processes.

Figure 8 shows the differences between the sensitivity experiment and the respective control runs for the peak and decay phases of the forced events. For each forced warm event the peak and decay phases are defined and corresponding anomalies to the control run are calculated. It can be seen that SST anomalies during the peak phase of the APR events are about twice as strong compared to JAN events (Fig. 8a). This leads to stronger reactions in short-wave radiation and latent heat flux. Increased SSTs lead to enhanced latent heat flux, which provides the main atmospheric damping. Latent heat fluxes are enhanced by 10% and 25% for JAN and APR, respectively (Fig. 8c). On the other hand, short-wave radiation shows consistent positive anomalies for both seasons, but these only account for 3% and 11% of the climatological values of the respective seasons. In total the heat flux changes offset each other and do not lead to any significant feedbacks. The precipitation anomalies caused by the warming, however, show a significant difference. The weaker warming in January/February causes stronger local precipitation anomalies compared to the April/May season (Fig. 8d). Also, the reduction of wind speed as a response to the warming is about 4 times stronger for the JAN events (not shown).

In none of the experiments, the coastal anomalies were self-contained through ocean-atmosphere feedbacks. We also do not observe any spreading of the anomalies further offshore than 90°W. Due to the shallow warming, the vertical temperature gradient increases drastically and allows the vertical advection to act as a strong damping once the forcing is switched off and upwelling velocities return to normal. The resulting weakened meridional wind is diminishing south of 5°S and upwelling intensity is hardly weakened. This suggests that for a longer-lasting event or events that spread into the equatorial Pacific, additional external forcing is necessary or the initial warming needs to also include the subsurface ocean to hinder vertical processes to rapidly dampen the warming.

6 Summary and discussion

In this study, we examined the seasonal cycle of the mixed layer heat budget in the region where Coastal Niño events take place, i.e. the far eastern tropical Pacific. We find that the seasonal cycle of mixed layer temperature mainly follows the seasonal cycle of the surface heat fluxes that act to warm the mixed layer throughout the year. Cooling is provided by subsurface processes and oceanic horizontal advection with the subsurface term being dominant. In tropical regions, solar radiation usually shows a semi-annual cycle. Off Peru, the combination with the annual cycle of cloudiness leads to an annual cycle of incoming solar radiation, which is the main driver of variations in the heat fluxes, highlighting the role of clouds for the Niño1 + 2 region.

Further, the cloudiness displays a strong seasonal cycle with varying cloud patterns between boreal spring (FMA) and the rest of the year due to the presence of the double ITCZ (Zhang 2001). This seasonal change in the cloud regime also leads to a reversal in the sign of the SST-cloud feedback. Hence, anomalous warming in boreal spring, i.e. the convective season, enhances cloudiness while it decreases cloudiness during the rest of the year.

This study highlights the uniqueness of the 2017 Coastal Niño event. Consistent with Garreaud (2018), our analysis suggests that surface heat fluxes have played a substantial role in creating the warming. For all other events found in the reanalysis data, surface heat fluxes only played a secondary role or were not important at all. Additionally, the 2017 event took place roughly three months earlier than other Stand-Alone Coastal Niño events. We argue here that this is crucial not only for its impact on precipitation but

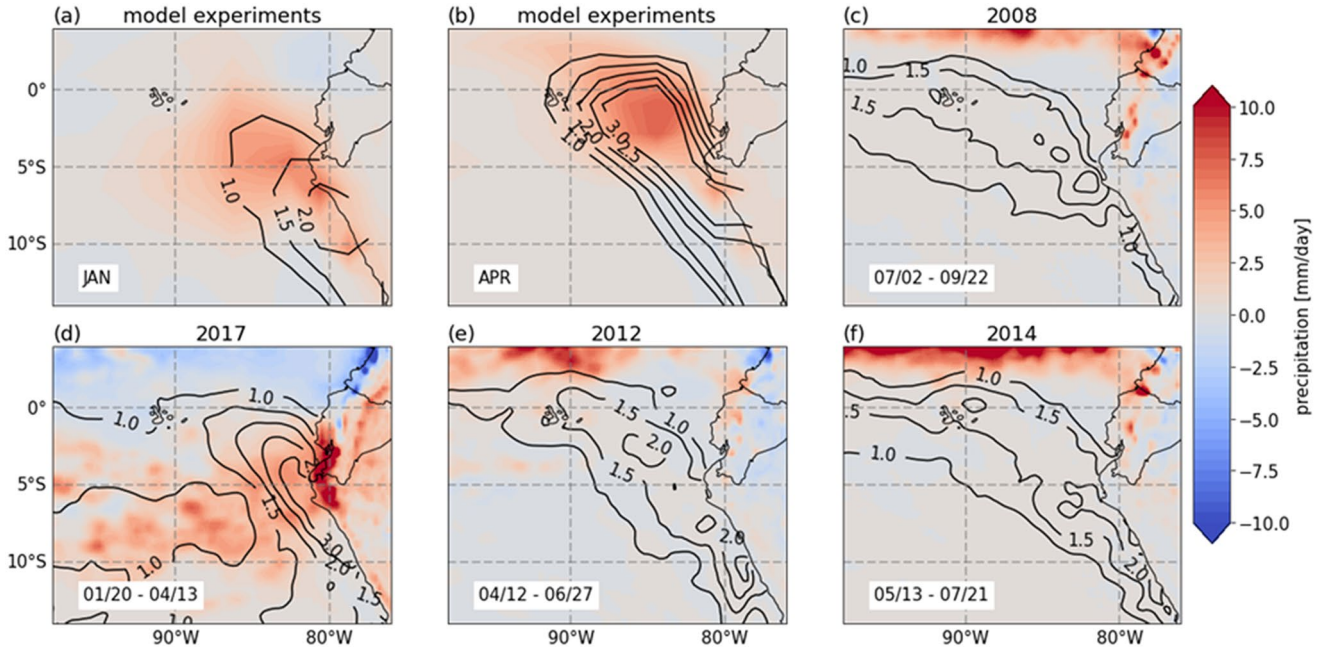

Fig. 9 Spatial patterns of SST (contours) and precipitation (shading) anomalies during the peak phases of the different events. **a**) and **b**) show composites of model sensitivity experiments while **c**) to **f**) display the observed events

also for its development as different mechanisms are dominant during different seasons.

Our model sensitivity experiments suggest that in general wind stress forcing applied in January leads to weaker warming compared to a forcing applied in April. The wind stress relaxation leads to a shoaling of the mixed layer and reduced upwelling. Hence, the reduction of solar radiation absorbed within the mixed layer damps the warming process, caused by drastically decreased cooling via subsurface processes. In January/February the mixed layer heat budget is dominated by the surface heat fluxes, which are not directly affected by the applied wind stress forcing in the model sensitivity experiments. Forced changes in the subsurface processes (i.e. upwelling) have less influence on SST in January/February compared to April/May when subsurface cooling dominates over surface fluxes in the mixed layer heat budget.

Several studies have suggested that coastal wind forcing was crucial for the development of the 2017 event. While Echevin et al. (2018) pointed out that the local wind stress forcing was the main driver, Peng et al. (2019) argued that Kelvin wave forcing contributed equally in 2017. Both studies, however, agree that Kelvin waves alone cannot produce an extreme event as observed in 2017 and that an interplay of Kelvin waves and northerly coastal wind anomalies is necessary. It has been suggested that Kelvin waves have a stronger coastal effect if forced in the eastern Pacific rather than the central western Pacific (Zhao and Karamperidou 2022). The results presented in this study agree with the findings of Takahashi and Martínez (2019) who noted that for the 1925 event surface heat flux and horizontal advection are the main drivers. They further emphasized that the seasonality was critical for the warming to provoke strong feedbacks.

The definition of coastal Niño events used in this study also accounts for rather short events but at the same time focuses on Stand-Alone events that are not connected to basin-wide El Niño events. In agreement with Hu et al. (2019), we find high variability within those events, both in the small number of observed as well as the simulated events. Our study thus highlights that there is no canonical coastal Niño event as strength, duration and forcing mechanism are highly variable. The seasonality is crucial for very strong events such as 1925 or 2017, as strong atmospheric feedbacks can only be triggered when climatological SSTs are close to the convective threshold. Further, the model sensitivity experiments show spatial differences in the precipitation patterns between the seasons. The JAN events, where the SST anomaly is constrained to the coastal region south of 5°S, lead to enhanced precipitation at 5°S right at the Peruvian coast, whereas APR events cause enhanced precipitation at around 2°S further offshore centred around 85°W (Fig. 9a, b). Thus, while the precipitation response for the APR events is of similar strength as for JAN, it falls mainly over the ocean. Indeed, anomalous precipitation directly along the coast (0°-10°S; 78°W-82°W) is significantly stronger in JAN events (2.11 mm/day) compared to APR events (1.27 mm/day). Similar differences in the

spatial warming and precipitation patterns can be seen for the observed events (Fig. 9c-f). The 2017 event shows the strongest warming between 5°S and 10°S and the maximum precipitation right at the coastal area of northern Peru and southern Ecuador. For the coastal Niños in 2008, 2012 and 2014, the warming is more spread towards the equator and the coastal intensification is less pronounced. The rainfall patterns further show little precipitation anomalies in the Niño1 + 2 region or over Peru and Ecuador. Strong anomalies are only visible at around 5°N and west of 85°W, suggesting rather a southward extension of the ITCZ than local convective rainfall.

Model experiments presented in this study show that wind stress-forced surface warming does not trigger enough atmospheric feedbacks to sustain itself. All forced events diminish rapidly after the forcing period as the surface warming increases the vertical temperature gradient and hence leads to very effective cooling once the upwelling returns. The warming events in January, however, show a relatively stronger response in precipitation (Figs. 8d and 9a and b). Thus, we conclude that warming events earlier in the year are more likely to be sustainable or reinforced, but in general additional forcing (e.g. via Kelvin waves) is necessary for 2017-like events.

Authors' contributions DR, SW and JFL conceived and designed the study. Model sensitivity experiments were performed by DR and SW. Analyses were performed by DR. The first version of the draft was written by DR and all authors commented on previous versions of the manuscript. All authors read and approved the final manuscript.

Funding Open Access funding enabled and organized by Projekt DEAL.
This study was funded by the Deutsche Forschungsgemeinschaft (DFG, German Research Foundation) as part of the PaCoNi project (Project ID 464487142).

Data availability Raw model output of the historical runs and the model sensitivity experiments is available from the long term archive at the Kiel University supercomputer. The ERA5 data used in this study can be found at https://cds.climate.copernicus.eu/cdsapp#!/dataset/reanalysis-era5-single-levels%3Ftab=form. The GLORYS data is publicly available at https://data.marine.copernicus.eu/product/GLOBAL_MULTIYEAR_PHY_ENS_001_031/services. Derived data and code are publicly accessible via https://doi.org/10.5281/zenodo.10808890.

Declarations

Competing interests The authors have no relevant financial interests to disclose.

References

Barnier B, Madec G, Penduff T, Molines JM, Treguier AM, Sommer JL, Beckmann A, Biastoch A, Böning C, Dengg J, Derval C, Edmée Durand, Sergei Gulev, Elizabeth Remy, Claude Talandier, Sébastien Theetten, Mathew Maltrud, Julie McClean, Beverly De Cuevas (2006) Impact of partial steps and momentum advection schemes in a global ocean circulation model at Eddy-permitting resolution. Ocean Dyn 56(5–6):543–67. https://doi.org/10.1007/s10236-006-0082-1

Biastoch A, Böning CW, Getzlaff J, Molines JM, and Gurvan Madec (2008) Causes of International-Decadal Variability in the Meridional Overturning Circulation of the Midlatitude North Atlantic Ocean. J Clim 21(24):6599–6615. https://doi.org/10.1175/2008JCLI2404.1

Bjerknes J (1969) Atmospheric teleconnections from the equatorial pacific, vol 97

Brink KH, Halpern D, Huyer A, Smiths RL (1983) The physical environment of the Peruvian upwelling system, vol 12

Brovkin V, Raddatz T, Reick CH, Claussen M, and Veronika Gayler (2009) Global biogeophysical interactions between forest and climate. Geophys Res Lett 36(7). https://doi.org/10.1029/2009GL037543

Cesana, Grégory DA, Del Genio S, Andrew Ackerman M, Kelley G, Elsaesser M, Ann Fridlind Y, Cheng, and Mao Sung Yao (2019) Evaluating Models Response of Tropical Low Clouds to SST Forcings Using CALIPSO Observations. Atmos Chem Phys 19(5):2813–2832. https://doi.org/10.5194/acp-19-2813-2019

Chavez FP, Messié M (2009) A Comparison of Eastern Boundary Upwelling Ecosystems. Prog Oceanogr 83(1–4):80–96. https://doi.org/10.1016/j.pocean.2009.07.032

Cronin MF, Nicholas A, Bond CW, Fairall, Weller RA (2006) Surface cloud forcing in the east pacific stratus deck/cold tongue/ITCZ complex*. https://doi.org/10.1175/JCLI3620.1

de Szoeke SP, Christopher W, Fairall DE, Wolfe L, Bariteau, and Paquita Zuidema (2010) Surface Flux Observations on the Southeastern Tropical Pacific Ocean and Attribution of Sst Errors in Coupled Ocean-Atmosphere Models. J Clim 23(15):4152–4174. https://doi.org/10.1175/2010JCLI3411.1

Echevin V, Colas F, Espinoza-Morriberon D, Vasquez L, Anculle T, Dimitri Gutierrez (2018) Forcings and evolution of the 2017 coastal El Niño Off northern Peru and Ecuador. Front Mar Sci 5(OCT). https://doi.org/10.3389/fmars.2018.00367

Foltz GR, Hummels R, Dengler M, Perez RC, and Moacyr Araujo (2020) Vertical turbulent cooling of the mixed layer in the atlantic ITCZ and trade wind regions. J Geophys Res Oceans 125(2). https://doi.org/10.1029/2019JC015529

Garreaud RenéD (2018) A Plausible Atmospheric Trigger for the 2017 Coastal El Niño. Int J Climatol 38:e1296–1302. https://doi.org/10.1002/joc.5426

Gu G, Adler RF, Sobel AH (2005) The eastern pacific ITCZ during the boreal spring

Harrison DE, Larkin NK (1998) El Nino-Southern Oscillation Sea Surface Temperature and Wind Anomalies, 1946–1993. Rev Geophys 36(3):353–399. https://doi.org/10.1029/98RG00715

Hersbach H, Bell B, Berrisford P, Biavati G, Horányi A, Muñoz Sabater J, Nicolas J, Peubey C, Radu R, Rozum I, Schepers D, Simmons A, Soci C, Dee D, Thépaut JN (2023) ERA5 hourly data on single levels from 1940 to present. Copernicus Climate Change Service (C3S) Climate Data Store (CDS).

Hu Z, Zhen B, Huang J, Zhu A, Kumar, and Michael J. McPhaden (2019) On the Variety of Coastal El Niño Events. Clim Dyn 52(12):7537–7552. https://doi.org/10.1007/s00382-018-4290-4

L'Heureux ML, Takahashi K, Watkins AB, Barnston AG, Becker EJ, Liberto TED, Gamble F, Gottschalck J, Halpert MS, Boyin Huang, Kobi Mosquera-Vásquez, and, Wittenberg AT (2017) Observing and predicting the 2015/16 El Niño. Bullet Am Meteor Soc 98(7):1363–82. https://doi.org/10.1175/BAMS-D-16-0009.1

Lübbecke JF, Rudloff D, Lothar S (2019) Stand-Alone Eastern Pacific Coastal Warming Events. Geophys Res Lett 46(21):12360–12367. https://doi.org/10.1029/2019GL084479

Ma C-C, Mechoso CR, Robertson AW, Arakawa A (1996) Peruvian stratus clouds and the tropical pacific circulation: a coupled Ocean-atmosphere GCM study. J Clim, 1635–1645. https://doi.org/10.1175/1520-0442(1996)009%3C1635:PSCATT%3E2.0.CO;2

Madec G (2016) NEMO ocean engine Gurvan Madec, and the NEMO team. https://doi.org/10.5281/zenodo.3248739

Matthes K, Biastoch A, Wahl S, Harlaß J, Martin T, Brücher T, Drews A, Ehlert D, Getzlaff K, Krüger F, Rath W, Scheinert M, Schwarzkopf FU (2020) Tobias Bayr, Hauke Schmidt, and Wonsun Park. The Flexible Ocean and Climate Infrastructure Version 1 (FOCI1): Mean State and variability. Geosci Model Dev 13(6):2533–68. https://doi.org/10.5194/gmd-13-2533-2020

McPhaden MJ, Timmermann A, Widlansky MJ, Balmaseda MA, and Timothy N. Stockdale (2015) The Curious Case of the El Niño That Never Happened: A Perspective from 40 Years of Progress in Climate Research and Forecasting. Bull Am Meteorol Soc 96(10):1647–1665. https://doi.org/10.1175/BAMS-D-14-00089.1

Montes I, Colas F, Capet X, and Wolfgang Schneider (2010) On the pathways of the equatorial subsurface currents in the eastern equatorial pacific and their contributions to the Peru-Chile undercurrent. J Geophys Res Oceans 115(9). https://doi.org/10.1029/2009JC005710

Moreno-Chamarro E, Caron LP, Tomas SL, Vegas-Regidor J, Gutjahr O, Moine MP, Putrasahan D, Roberts CD, Roberts MJ Retish Senan, Laurent Terray, Etienne Tourigny, and Pier Luigi Vidale (2022) Impact of increased resolution on long-standing biases in highResMIP-PRIMAVERA climate models. Geosci Model Dev 15(1):269–289. https://doi.org/10.5194/gmd-15-269-2022

Müller WA, Jungclaus JH, Mauritsen T, Baehr J, Bittner M, Budich R, Bunzel F, Esch M, Ghosh R, Haak H, Ilyina T, Kleine T, Kornblueh L, Li H, Modali K, Notz D, Pohlmann H, Roeckner E, Stemmler I, Tian F, Marotzke J (2018) A Higher-Resolution Version of the Max Planck Institute Earth System Model (MPI-ESM1.2-HR). J Adv Model Earth Syst 10(7):1383–1413. https://doi.org/10.1029/2017MS001217

Neelin J, David DS, Battisti AC, Hirst FF, Jin Y, Wakata T, Yamagata, Zebiak SE (1998) ENSO Theory. J Geophys Research: Oceans 103(C7):14261–14290. https://doi.org/10.1029/97jc03424

Peng Q, Xie SP, Wang D, Zheng XT, and Hong Zhang (2019) Coupled ocean-atmosphere dynamics of the 2017 extreme coastal El Niño. Nat Commun 10(1). https://doi.org/10.1038/s41467-018-08258-8

Ramírez IJ, Fernando Briones (2017) Understanding the El Niño Costero of 2017: The Definition Problem and Challenges of Climate Forecasting and Disaster Responses. Int J Disaster Risk Sci 8(4):489–492. https://doi.org/10.1007/s13753-017-0151-8

Reick CH, Raddatz T, Brovkin V, Gayler V (2013) Representation of Natural and Anthropogenic Land Cover Change in MPI-ESM. J Adv Model Earth Syst 5(3):459–482. https://doi.org/10.1002/jame.20022

Richter I (2015) Climate Model Biases in the Eastern Tropical Oceans: Causes, Impacts and Ways Forward. Wiley Interdisciplinary Reviews: Clim Change 6(3):345–358. https://doi.org/10.1002/wcc.338

Stevens B, Giorgetta M, Esch M, Mauritsen T, Crueger T, Rast S, Salzmann M, Schmidt H, Bader Jürgen, Block K, Brokopf R, Fast I, Kinne S, Kornblueh L, Lohmann U, Pincus R, Reichler T, and Erich Roeckner (2013) Atmospheric Component of the MPI-M Earth System Model: ECHAM6. J Adv Model Earth Syst 5(2):146–172. https://doi.org/10.1002/jame.20015

Takahashi K, Martínez AG (2019) The Very Strong Coastal El Niño in 1925 in the Far-Eastern Pacific. Clim Dyn 52(12):7389–7415. https://doi.org/10.1007/s00382-017-3702-1

Thoma M, Gerdes R, Greatbatch RJ, Ding H (2015) Partially Coupled Spin-up of the MPI-ESM: Implementation and First Results. Geosci Model Dev 8(1):51–68. https://doi.org/10.5194/gmd-8-51-2015

Timmermann A, An S-I, Kug J-S, Jin F-F, Cai W, Capotondi A, Cobb KM, Lengaigne M, McPhaden MJ, Malte F, Stuecker K, Stein AT, Wittenberg K-S, Yun T, Bayr H-C, Chen Y, Chikamoto B, Dewitte J-Y, Lee T, Li J-J, Luo, Shayne McGregor, Yann Planton, Scott Power, Harun Rashid, Hong-Li Ren, Agus Santoso, Ken Takahashi, Alexander Todd, Guomin Wang, Guojian Wang, Ruihuang Xie, Woo-Hyun Yang, Sang-Wook Yeh, Jinho Yoon, Elke Zeller, Zhang X (2018) El Niño–Southern oscillation complexity. Nature 559(7715):535–45. https://doi.org/10.1038/s41586-018-0252-6

Valcke S (2013) The OASIS3 Coupler: A European Climate Modelling Community Software. Geosci Model Dev 6(2):373–388. https://doi.org/10.5194/gmd-6-373-2013

Xie SP, Philander SGH (1994) A coupled ocean-atmosphere Model of Relevance to the ITCZ in the Eastern Pacific. Tellus A 46(4):340–350. https://doi.org/10.1034/j.1600-0870.1994.t01-1-00001.x

Zhang C (2001) Double ITCZs. J Geophys Res Atmos 106(D11):11785–11792. https://doi.org/10.1029/2001JD900046

Zhao S, Karamperidou C (2022) Competing effects of eastern and central-western pacific winds in the evolution of the 2017 extreme coastal El Niño. Geophys Res Lett 49(15). https://doi.org/10.1029/2022GL098859